ADVANCED MATERIALS
www.advmat.de

Fully Recyclable Pluripotent Networks for 3D Printing Enabled by Dissociative Dynamic Bonds

Marco Caliari, Fernando Vidal, Daniele Mantione, Guillem Seychal, Mariano Campoy-Quiles, Lourdes Irusta, Mercedes Fernandez, Xabier Lopez de Pariza, Thomas Habets, Nora Aramburu, Jean-Marie Raquez, Bruno Grignard, Alejandro J. Müller, Christophe Detrembleur, and Haritz Sardon**

Additive manufacturing (AM) has risen in popularity due to its ability to produce complex shapes in a material-efficient way. However, to produce objects with advanced properties, complex multimaterial strategies are often employed. This one-polymer-one-property paradigm significantly slows down the application of AM, and in particular of fused deposition modeling (FDM), for manufacturing of functional objects. In this study advantage of pluripotency in materials is taken, i.e., the ability to attain different properties from a single stock, to afford mechanically tunable 3D printed dynamic thermosets (moduli from 2 MPa – 3 GPa, 1500× increase, Stress at break from 2 to 70 MPa, 35× increase). To do so, FDM-compatible CO_2-derived dissociative polymer networks are designed that undergo a dynamic reaction-induced phase-separation (DRIPS). This strategy enables the control of the size of the rigid phase with a simple post-printing thermal treatment, cascading in spatially patterned mechanical properties. This study showcases new directions for the 3D printing communities, with deep implications in soft robotics and compliant mechanics.

1. Introduction

Additive manufacturing (AM), commonly named 3D printing, has evolved from a small-size and rapid prototyping technique to full-scale manufacturing tool widely applied in fields[1,2] ranging from automotive,[3] construction to biomedical.[4,5] Of all the 3D printing methods, fused deposition modeling (FDM) stands out for its simplicity, safety, and broad range of resulting materials properties.[6,7] In FDM, thermoplastic materials are melted through a heated nozzle and transformed into a 3D object by depositing the melt filament in a layer-by-layer fashion. However, the potential of FDM suffers from the anisotropic mechanical properties of the prints due to the poor interfilamentous adhesion as the different layers are bonded only by weak non-covalent forces.[8,9]

Among the different approaches to reduce the anisotropy while maintaining the sustainability of FDM, the introduction of dynamic cross-links is one of the most promising strategy.[10–13] A judicious choice of the dynamic bond enabled the extrusion of networks based on the transesterification reaction,[14–16] disulfide metathesis,[17] imine exchange,[18] thiol anhydride exchange[19] and Diels alder

M. Caliari, F. Vidal, D. Mantione, G. Seychal, L. Irusta, M. Fernandez, X. L. de Pariza, N. Aramburu, A. J. Müller, H. Sardon
POLYMAT and Department of Polymers and Advanced Materials: Physics Chemistry and Technology
Faculty of Chemistry
University of the Basque Country UPV/EHU
Paseo Manuel de Lardizábal 3, Donostia-San Sebastián 20018, Spain
E-mail: haritz.sardon@ehu.eus

M. Caliari, T. Habets, B. Grignard, C. Detrembleur
Center for Education and Research on Macromolecules (CERM)
CESAM Research Unit
University of Liege
Sart-Tilman B6a, Liege 4000, Belgium
E-mail: christophe.detrembleur@uliege.be

The ORCID identification number(s) for the author(s) of this article can be found under https://doi.org/10.1002/adma.202417355

DOI: 10.1002/adma.202417355

D. Mantione, A. J. Müller
Ikerbasque
Basque Foundation for Science
Plaza Euskadi 5, Bilbao 48009, Spain

G. Seychal, J.-M. Raquez
Laboratory of Polymeric and Composite Materials
Center of Innovation and Research in Materials and Polymers (CIRMAP)
University of Mons
Place du Parc 23, Mons 7000, Belgium

M. Campoy-Quiles
Institute of Materials Science of Barcelona
ICMAB-CSIC
Campus UAB, Bellaterra 08193, Spain

J.-M. Raquez, C. Detrembleur
WEL Research Institute
Avenue Pasteur 6, Wavre 1300, Belgium

B. Grignard
FRITCO2T Platform
University of Liege
Sart-Tilman B6a, Liege 4000, Belgium

reaction,[20–22] thus opening the doors to their use in FDM processes.[7,8,21] As an example, Smaldone and co-workers proposed a ground-up design of a dissociative network specifically designed for FDM showing isotropy up to 95% enabled by its high degree of cross-linking.[20] Despite of the achievement of isotropic prints, these new materials needed long cooling times due to the slow recovery of cross-links and were printed with a custom-built 3D printer. While the incorporation of these dynamic bonds does not impede their "drop-in" in current 3D printers, the introduction of a high density of cross-links in long chain polymers can dramatically change their processing parameters. This may result in thermal degradation side reactions and high viscosities that hinder printability.[20]

A recent progress in the field of dissociative networks, pluripotency, i.e., the ability to attain different properties from a single material, has been translated to the chemical space by Rowan and coworkers. In their work, they took advantage of the dynamic reaction-induced phase-separation (DRIPS) as an efficient strategy to tune the properties of polymeric materials.[23–26] We envision that combining adequate DRIPS morphologies, room-temperature exchange dynamics, thermal transitions ($T_{ambient} < T_g < T_{annealing} < T_{Upper\ Transition}$, T_{UT}), and melt viscoelastic properties, would result in a powerful platform for the additive manufacturing of complex actuators with on demand mechanical properties from a single material, a feat that is achieved in light-based 3D printing but not in FDM.[27–29] We decided to employ FDM printing as it is a more commonly-available technique, requires little specialized equipment and would benefit majorly from the introduction of single material-multiple properties strategies. To advance pluripotency into FDM, thus introducing spatially-resolved properties from a single material, three design criteria must be fulfilled: i) appropriate melt viscosities at high temperatures; ii) a wide "tempering" window, where the cross-linking density (i.e., the ratio at equilibrium of an open/close adduct) can be thermally modulated and topologically fixed once cooled at room temperature[26] and iii) a covalent bond possessing fast reversibility at processing temperatures, which enables hot filament extrusion without incurring in melt-fracture, a common issue when working with CANs.[17] Applying this concept could be a further evolution in FDM 3D printing as the mechanical properties of the objects could evolve after printing by simple and localized annealing.[26] This could avoid other multi-material strategies for the production of complex, functional structures.[7,30–32]

In our search for a dynamic bond that could be amenable for pluripotency, we paid special attention to the dialkyl-substituted *N,S*-acetal group in cyclic oxazolidones. It was previously demonstrated that the reaction of terminal thiols with the exo-vinylene group (>C=CH_2) of alkylidene oxazolidones has indeed a quick association-dissociation dynamics below 50 °C and low activation barriers of exchange (≈16–19 kcal mol^{-1}) under catalytic amounts of methyl sulfonic acid (MSA).[33,34] Furthermore, this bond is sufficiently rigid ($T_g > T_{ambient}$) and had previously provided materials with high transparency, no coloration or odor, a set of improved characteristics compared to other networks containing linear thioethers produced by radical thiol-ene or (anion-mediated) thia-Michael reactions.[35–37] However, networks comprising only reversible *N,S*-acetal bonds as cross-linking points undergo thermal depolymerization into monomeric fragments at low temperatures (<100 °C), resulting in rapid loss of mechanical performance and melt viscosities unfit for FDM (**Figure 1**a,d). We hypothesized that balancing network integrity and dynamicity by combining permanent/dynamic cross-links would enable the implementation of high-performance poly(oxazolidone)-type materials[33,38–44] into simultaneously pluripotent and 3D printable objects.

To achieve this, we designed a monomer structure that forms permanent and dynamic bonds through two concurrent reactions. We propose a bifunctional oxazolidone monomer, 3-allyl-5,5-dimethyl-4-methyleneoxazolidin-2-one (**AllOx**, Figure 1), containing two C=C double bonds with divergent reactivities. The monomer is highly scalable and composed of 26 wt.% of carbon dioxide (CO_2), making use of this widely available C1 synthon.[45–47] In contrast, most polymer networks today that combine strong and weak bonds necessitate multiple tailored monomers or complex architectures. This strategy would greatly simplify this conundrum by enabling the introduction of dynamic and permanent bonds from a single source,[48] reminiscent to one-monomer two-polymer systems.[49,50] We further demonstrate how photo-radical and photo-acid initiators are efficient UV photocuring agents to simultaneously, or in "tandem", trigger both radical and cationic pathways of AllOx, giving rise to both thermally labile and irreversible network nodes homogeneously distributed in the bulk material (Figure 1b,c). More importantly the "tandem" networks present a marked (sub) microphase-segregation via DRIPS mechanism, affording mechanically strong and tunable materials (from elastomeric to rigid and ductile to stiff and brittle, Young's moduli (E_Y) = 2 MPa – 3 GPa, 1500x increase) that can be controlled by a thermal annealing process, with suitable viscoelastic profiles for FDM and mechanical reprocessability (Figure 1e). We show that we can afford single-material 3D printed objects with spatially resolved mechanical properties and isotropy showcasing new possible directions for FDM 3D printing, with potential to actuate in soft-robotics and compliant mechanics.

2. Probing Thiol-Ene Reactions in a Difunctional Oxazolidone

The modular, highly scalable, and highly atom economical (AE = 0.87) synthesis of functional oxazolidones enabled us to access the desired **AllOx** monomer in >100-gram batches (78% yield) directly from CO_2. Our adapted 1-step protocol reaction between a propargyl alcohol, allyl amine, and CO_2 employed readily available commercial starting materials and a cheap, heterogenous CuI catalyst (**Figure 2**a).[47] The targeted transparent and liquid monomer could be easily dehydrated and purified in a distillation apparatus, overall providing an convenient preparation route for the broader applicability of **AllOx** (see Supporting Information for experimental details, Figures S1and S2, Supporting Information).

With the new allyl-alkylidenyl-oxazolidone monomer in hand, we set to probe the chemoselectivity of the radical versus cationic thiol-ene processes toward the two distinct C=C functional groups. Formation of the three possible S–C bonds (two thioether via radical pathways, Figure S3a (Supporting Information); one *N,S*-acetal via cationic pathways Figure S3b, Supporting Information)[35] was followed by sampling reactions in bulk

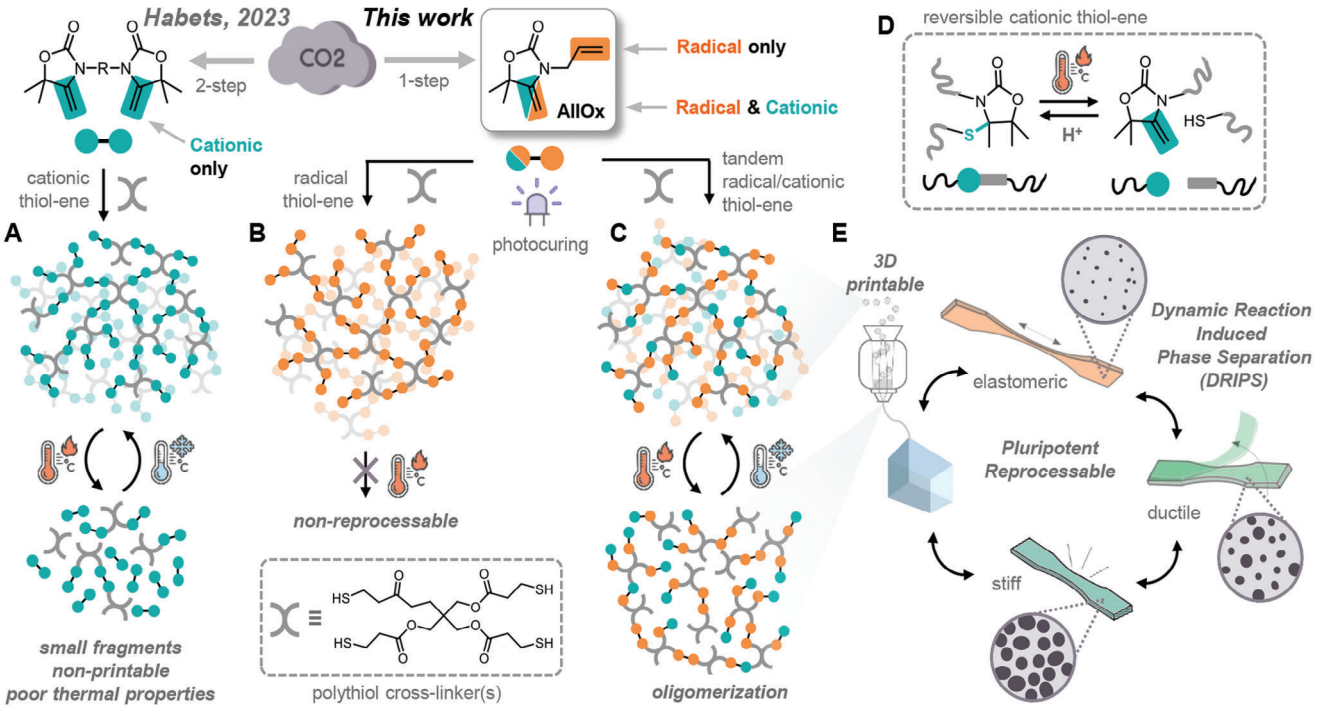

Figure 1. General strategy to attain pluripotent CO_2-derived oxazolidone-based polymer networks exploiting permanent/reversible thiol-ene reactions with polythiol cross-linkers: bridged bis-oxazolidone monomers with two identical exo-vinylene groups as studied by Habets et al. (2023) formed fully depolymerizable networks via exclusive cationic thiol-ene reactions (a); a diolefinic oxazolidone monomer (**AllOx**) photocured into two distinct polymer networks by choice of initiation: a photo-radical initiator created fully permanent and non-reprocessable networks (b), while a "tandem" combination of radical/cationic initiators generated a mix of permanent/dynamic bonds (c). Scheme of the reversible cationic thiol-ene (d). Thermally depolymerizable photocured resins via tandem thiol-ene displayed dynamic reaction-induced phase separation (DRIPS), which can be exploited to produce 3D printable and reprocessable materials with pluripotent characteristics, ranging from elastomeric, ductile, and stiff (e).

using 3-methyl mercaptopropionate (3MP) as a model monofunctional aliphatic thiol (Figure 2, see Supporting Information for details). As expected, conversion data as measured by ^{1}H NMR analyses demonstrated that the chemoselectivity of the process strongly depended on the type of initiation. In the presence of isopropyl thioxanthone (ITX, 1 wt.%) as an efficient type II photoinitiator (PI) under UV irradiation (390 nm),[51] the reaction of the model thiol lacked complete chemoselectivity toward the allyl and exovinylene C=C double bonds over an extended period of time (Figure 2b; Figures S4 and S9, Supporting Information). In the NMR spectra, the formation of two thioether groups was evident by the disappearance of the resonances associated with the olefinic groups (δ = 5.71, 5.18 ppm for allyl, 4.04 ppm for exo-vinylene) and the appearance of new –CH_2S– peaks (δ = 3.55, 3.24, 2.9-2.7, and 1.88 ppm) (Figure 2c; Figure S5, Supporting Information). However, the reaction rates differed significantly at room temperature: within 2 min of UV irradiation, 86% of the allyl group had reacted while conversion of the exo-vinylene group had only reached 7% (Figure 2b), suggesting that complementary reaction pathways could be possible at short reaction times. Using phenylbis(2,4,6-trimethylbenzoyl) phosphineoxide (BAPO, 1 wt.%) as PI under equivalent conditions resulted in similar reactivity, albeit higher conversions of the exo-vinylene group were achieved at long reaction times (Figure 5; Figures S10 and S11, Supporting Information). The structure of the double thiol-ene radical adduct (**OX_S1**) was supported by ^{1}H, ^{13}C NMR and high-resolution mass-spectrometry (HRMS) characterization of the isolated species (Figure S5, Supporting Information).

Next, we investigated the cationic thiol-ene pathway between **AllOx** and 3MP using methanesulfonic acid (MSA) as catalyst (Figure S3b, Supporting Information, mechanism). MSA was selected as was previously demonstrated to efficiently catalyze the cationic thiol/ene reaction.[52] As expected, we observed a high chemoselectivity toward the exovinylene moiety, leaving the allyl C=C unreacted after 40 min at room temperature (Figure 2d; Figure S11, Supporting Information).[35] Specifically, the ^{1}H NMR spectra displayed a rapid disappearance of the exovinylene peaks (δ = 4.04 ppm) while the allyl peaks shifted to higher ppm (δ = 5.71, 5.18 to 5.87, and 5.28–5.14 ppm) (Figure 2e; Figure S7, Supporting Information). Efficient formation of the *N,S*-acetal adduct (**OX_S2**) that reached 72% conversion after just 1 min, could also be followed by new –Me resonances (δ = 1.59, 1.40, 1.38 ppm).

Hence, to make use of the high selectivity toward distinct C=C at short periods of time, a fast "tandem" radical/cationic thiol-ene process –rather than a sequential one– needed to be devised. Inspired by previous acrylate-epoxy formulations for vat photopolymerization,[53–55] we investigated a combination of a photo-acid and a photoradical initiator to trigger both processes concomitantly with the switch ON of UV irradiation (≈390 nm). The system consisted of ITX as photosensitizer,

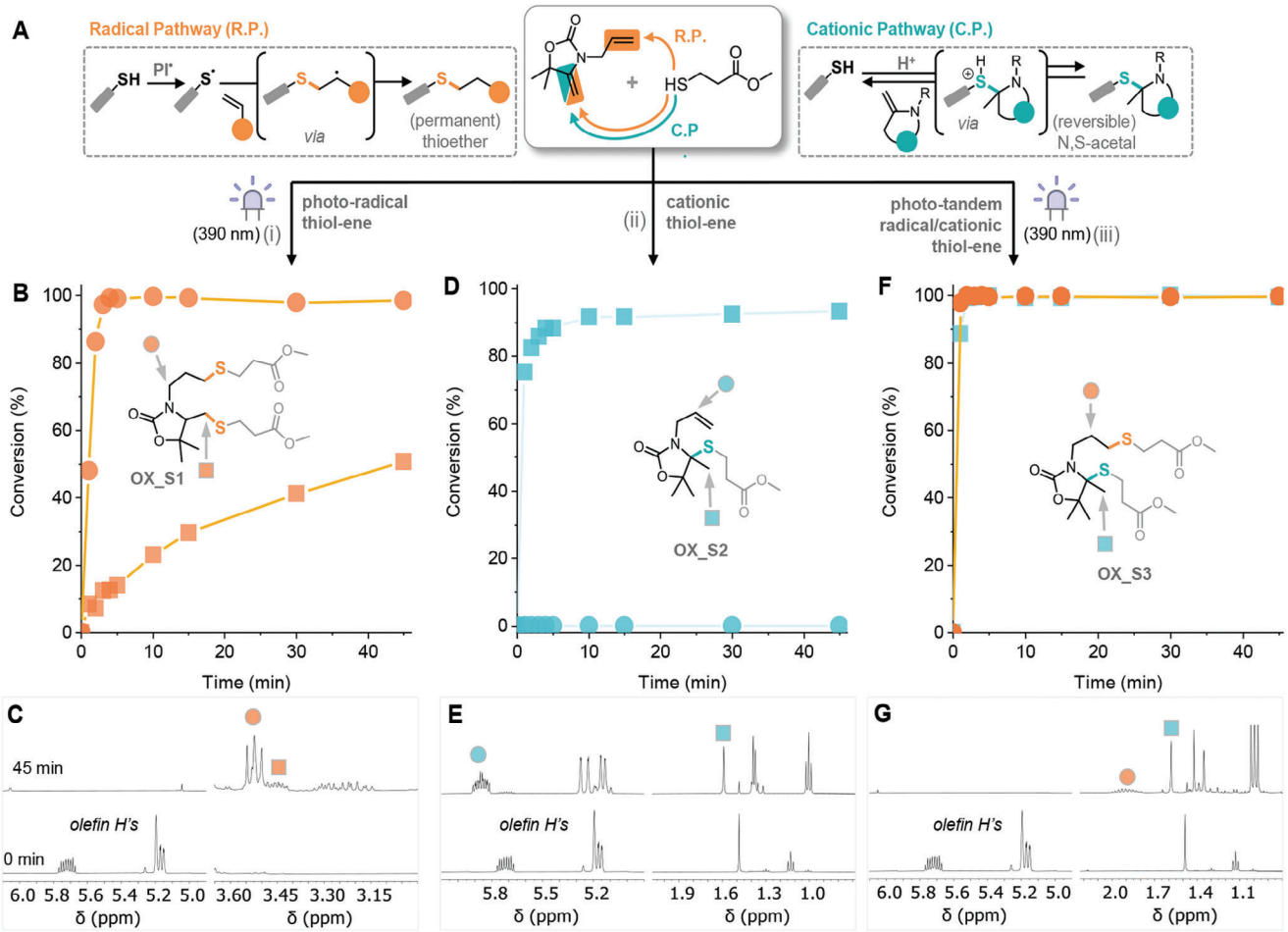

Figure 2. a) Model thiol-ene reaction studies and schematic representation of the radical and cationic pathways. Conversion data over time of the reaction between **AllOx** monomer and mono-functional thiol methyl 3-mercaptopropionate in bulk with various initiators as determined by ^{1}H NMR spectroscopy, following b) photo-radical thiol-ene to form bis-thioether model **OX_S1** and corresponding ^{1}H NMR (c), d) cationic thiol-ene to form N,S-acetal model **OX_S2** with unreacted allyl group (e); and f) photo-tandem radical/cationic thiol-ene to form thioether/N,S-acetal model **OX_S3** (g). Reagents and conditions (see Supporting Information for details): i) bulk, 1 mol% phenylbis(2,4,6-trimethylbenzoyl) phosphine oxide (BAPO), UV irradiation (390 nm), room temperature; ii) bulk, 1 mol% methanesulfonic acid (MSA), room temperature; iii) bulk isopropyl thioxanthone (ITX) and bis(4-methylphenyl) iodonium hexafluorophosphate (IOD) in 1:1 ratio 1 mol% UV irradiation (390 nm), room temperature. Corresponding 1H NMR spectra before and after 45 min of irradiation for radical (e), cationic (f) and tandem (g) kinetics.

which served as an efficient initiator for radical thiol-ene reaction (via H-abstraction of the thiol)[51] as well as to sensitize iodonium salts-based photoacids (in this work, bis(4-methylphenyl) iodonium hexafluorophosphate (IOD))[56,57] Indeed, employing 1 wt.% of the photosensitizer-photoacid ITX/IOD system in 1:1 weight ratio resulted in fast reaction kinetics and high conversions of both C=C double bonds in the same studied model reaction between **AllOx** and 3MP (Figure 2f; Figure S13, Supporting Information). Specifically, conversions of 99% and 85% according to the ^{1}H NMR spectra were attained for allyl and exo-vinylene groups, respectively, within 1 min at room temperature upon UV irradiation (390 nm). The simultaneous activation of both radical and cationic pathways was confirmed by the formation of the *N,S*-acetal and thioester adducts (**OX_S3**), which presented a new –CH_2S– peak (δ = 3.50–3.26 and 1.90 ppm,) and a new –Me peak (δ = 1.59, 1.43, 1.36 ppm), which could only form by the simultaneous radical and cationic pathways, respectively (Figure 2g; Figure S9, Supporting Information).

3. Reversible Thiol-Ene Dynamics in Tandem Polymer Networks

Once the reactivity of the **AllOx** monomer toward the radical and cationic thiol-ene pathways was established, the formation of polymer networks was investigated with equimolar amounts of tetrafunctional pentaerythritol tetrakis(3-mercaptopropionate) (**S4**). In such systems, we expected to control the extent of permanent thioether and reversible *N,S*-acetals linkages by the choice of initiator (radical vs tandem radical/cationic). In this way, we could probe the influence of cross-linking equilibrium thermodynamics (as reflected by DRIPS microstructures and extent of dynamic bonds formed) in governing bulk materials properties. Thus, we used 1 wt.% of the same photoradical (BAPO) or

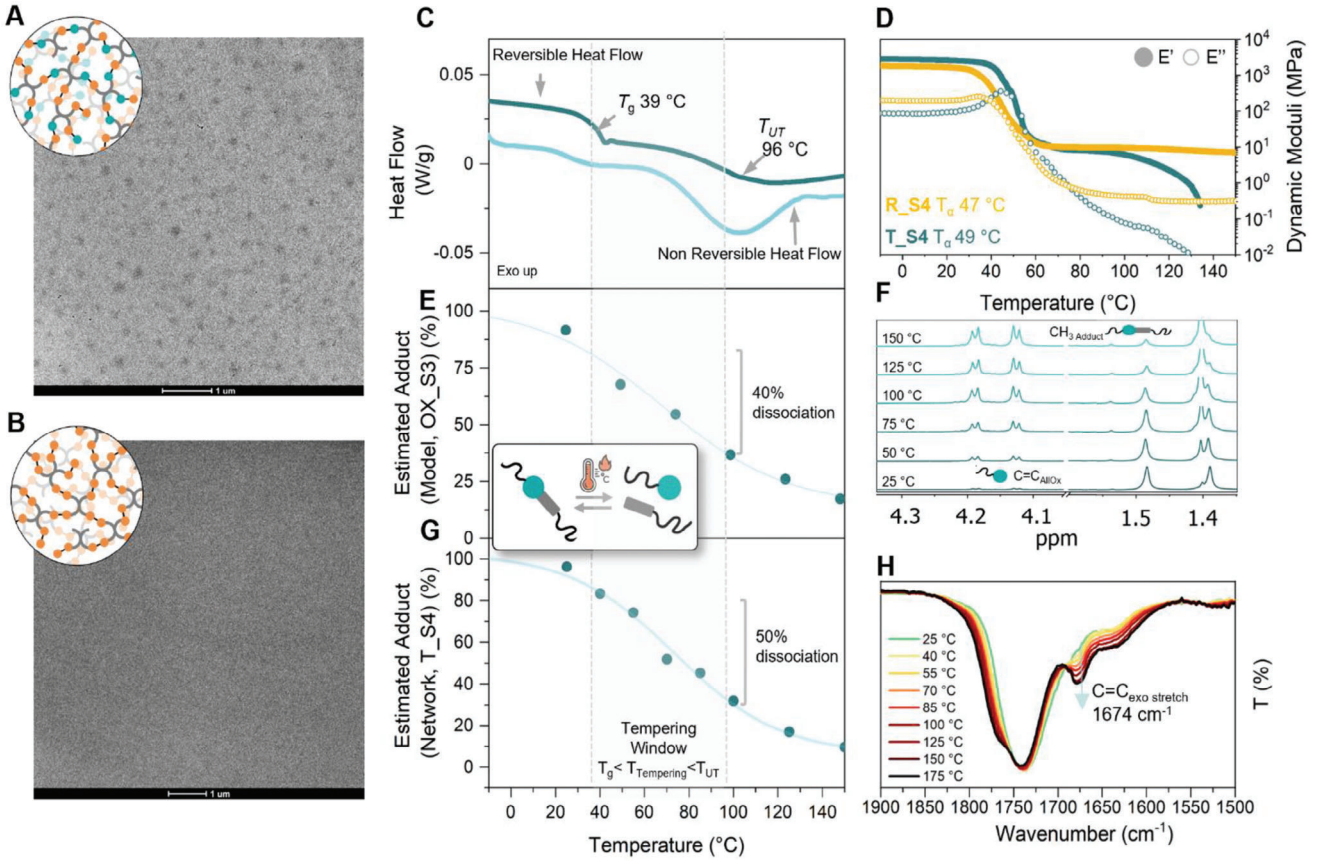

Figure 3. Transmission electron microscopy of dynamic "tandem" oxazolidone network, **T_S4**, showing a DRIPS microstructure (a), and permanent radical oxazolidone network, **R_S4**, without detectable features (b). (c) Reversing (teal) and non-reversing (cyan) mDSC thermograms of **TS_4**. (d) Dynamic mechanical analyses (DMA) of **T_S4** (teal) and **R_S4** (yellow). Overlap of thiol-ene reaction dynamics with polymer thermal transitions: extend of adduct formation in a molecular model **OX_S3** (e) as calculated from ^{1}H NMR experiments of dissociated adducts by treatment at different temperatures (f); extend of adduct formation in bulk **TS_4** polymer network (g) as determined from FT-IR experiments at 25 °C after thermal annealing at various temperatures. In situ temperature-dependent FTIR spectra of tandem material at temperatures between 25 and 175 °C (h).

tandem photosensitizer-photoacid system (ITX/IOD in 1:1 weight ratio) under otherwise similar conditions (bulk, 365 nm, room temperature, 30 min) to yield solid polymer networks **R_S4** and **T_S4**, respectively (Figure 1, further details on the preparation in Supporting Information). In both cases, complete consumption of the C=C double bonds was confirmed by the disappearance of the Fourier-transform infrared (FT-IR) resonances at 1678 and 1640 cm^{-1} corresponding to the stretching modes of the exo-vinylene and allyl groups, respectively (Figure S14, Supporting Information). Due to the low dipole of the C–S bonds, the new thioether and N,S-thioacetal bonds provided weak, non-conclusive signals in the FT-IR spectra of the isolated network. However, both materials showed gel contents above 90% in THF, confirming their cross-linked nature (Table S1, Supporting Information). The photocuring reaction kinetics were quick and efficient, reaching conversion of 80% with a 60 s irradiation (390 nm, 20 mW cm^{-2}) and having a gel point of 225 s (Figure S15, Supporting Information).

Despite the use of same monomeric building blocks, as well as seemingly identical C=C conversions (resulting in likely comparable network topologies), the distinct access to reversible cross-links between **R_S4** (permanent) and **T_S4** (dynamic) resulted in drastically different microstructures and thermal properties. First, a phase separated morphology was clearly present in analyses of tandem network **T_S4**, as observed by transmission electron microscopy (TEM) (**Figure 3a**) and optical microscopy (OM) (Figure S16, Supporting Information) All these results indicated areas of higher electron density and refractive index, attributed to hard domains (≈100 nm in size) in a continuous soft matrix conforming with a characteristic DRIPS microstructure. Although scanning near field optical microscopy (s-NOM) coupled with nano-FT-IR mapping and Confocal Raman Microscopy could not unambiguously distinguish chemical differences between the domain phases (Figures S17 and S18, Supporting Information), tracing the peak intensities at 977 and 1741 cm^{-1} revealed identical phase-separated structures as those observed by atomic force microscopy (AFM) (Figure S19, Supporting Information). In stark contrast, radically cross-linked network **R_S4** displayed no obvious features in neither TEM (Figure 3b) nor OM or AFM (Figures S16 and S20, Supporting Information), suggesting a single polymer matrix with spatial homogeneity in its cross-linking density.

Second, modulated differential scanning calorimetry (mDSC) analysis of **T_S4** showed two thermal transitions in the

reversing heat flow curves (T_g = 39 °C, T_{UT} = 96 °C, Figure 3c); the broader T_{UT} (which presented an onset at 69 °C) was accompanied by an endothermic peak in the non-reversing thermogram, a sign of the expected depolymerization reaction (vide infra). This temperature range provided ≈60 °C tempering window for developing the material's mechanical properties (that is, the temperature range between T_g and T_{UT}). In sharp contrast, **R_S4** displayed only one glass transition at slightly lower temperatures (T_g = 20 °C) and no endothermic peak in the non-reversing heat flow curve, further confirming the permanent nature of the radically cross-linked network (Figure S21, Supporting Information). The differences in thermal transitions observed by DSC were also paralleled in dynamic thermomechanical analyses (DMTA) of photocured rectangular strips (Figure 3d). In one hand, alpha relaxations, assigned to the T_g of the materials, could be observed in both networks (T_α = 47–49 °C). Contrarily, **T_S4** showed a 2-order of magnitude drop in the storage modulus (E') above 100 °C, while no changes in the plateau E' were observed in **R_S4** above 100 °C. Furthermore, **T_S4** showed a high but accessible $T_{depolymerization}$ (155 °C, Figure S22, Supporting Information) as determined by the final melt-flow of **T_S4** in a temperature ramp in a shear rheology, a beneficial property that points toward its possible FDM printability.

Having observed different outcomes in the physical properties between the two modes of network photocuring, we sought to demonstrate the reversible thiol-ene bond in **T_S4** as the acting mechanism. A combination of ex situ and in situ analyses by ^{1}H NMR and FT-IR spectroscopy (Figure 3e,h) provided convincing evidence of the cleavage of the thiol-ene adduct and formation of transient depolymerized structures, likely as a result of the residual protic species present upon photoacid activation. First, ex situ ^{1}H NMR spectroscopy experiments of isolated tandem model **OX_S3** treated at various temperatures (15 min) to activate the reversible *N,S*-acetal bond and quenched with base, akin to a material annealing process, revealed a ≈40% change in the dissociation of the *N,S*-acetal thiol-ene adduct between T_g and T_{UT} (Figure 3e,f; Figure S23, Supporting Information), similar to other non-catalyzed thia-Michael networks.[23,26] Specifically, new resonances of the alkylidene C=C in the parent **AllOx** (δ = 4.19–4.13 ppm) steadily appeared with concomitant reduction of the -Me signal of the *N,S*-acetal group (δ = 1.59, 1.43, 1.36 ppm) on raising the treatment temperature from 25 to 150 °C. The extent of dissociation was further supported by in situ FT-IR spectroscopy at temperatures from 25 to 150 °C of model network **T_S4**. As expected, the intensity of the exo-vinylene C=C double bond (1678 cm^{-1}) increased on heating, which also correlated to ≈50% change in the dissociation of the *N,S*-acetal thiol-ene adduct (Figure 3f,h). In contrast, radically photocured **R_S4** displayed negligible increase in FT-IR resonances associated with the alkylidene C=C when the material was subjected to an identical thermal study, attesting for its non-dissociative behavior (Figure S24a, Supporting Information). Importantly, the extent of the dissociated *N,S*-acetal thiol-ene adduct was at least partially preserved upon cooling to room temperature after the thermal treatment, as confirmed by FTIR spectroscopy (Figure S24b, Supporting Information).

Finally, **T_S4** was subjected to 150 °C for 10 min (>80% extent depolymerization), a point at which triethylamine was added to the resulting viscous liquid in order to quench the acid catalyst and thus, to avoid the back reaction (i.e., *N,S*-acetal formation) when cooling.[33] The partial solubility of this material in polar organic solvents allowed the spectroscopic and chromatographic characterization of the resulting oligomers. Specifically, ^{1}H and ^{13}C NMR analyses of the soluble fraction in DMSO-d_6 showed the presence of free exo-vinylene double bonds as indicated by the peaks at 4.22–4.16 and 150 ppm in the ^{1}H and ^{13}C NMR spectra, respectively (Figure S25, Supporting Information). Size exclusion chromatography (SEC) in tetrahydrofuran (THF) revealed oligomeric species with a number average molecular weight (M_w) of 1900 g.mol^{-1} and a dispersity ($Đ$) of 1.9 (Figure S26, Supporting Information). The presence of thio-ether bond linkages (δ = 3.63 ppm, CH) in the soluble fraction further confirmed at least partial step-growth polymerization via permanent radical thiol-ene, confirming that indeed both reactions occurred during tandem photocuring.

4. Attaining Pluripotent Behavior through Tempering

Having demonstrated the presence of DRIPS microstructures and the influence of temperature in the extent of thiol-ene adduct formation, we were intrigued by the effect of tempering in the observed phase separation and mechanical properties (**Figure 4a**). Hence, dumbbell shaped specimens (ASTM D638 TYPE V) were prepared by photocuring films of **T_S4**, treatment for 24 h at five different temperatures (40, 60, 75, 90, and 110 °C), and finally cut to shape with a sample die. AFM studies confirmed the sea-island type morphology with quasi-spherical domains embedded in a continuous matrix previously observed with TEM, s-NOM, and OM (Figure 4b; Table S2, Figures S14–S17, Supporting Information). Interestingly, samples tempered below the onset of T_{UT} at 40 and 60 °C showcased a significant increase in domain size (84, 152, and 168 nm at 25, 40, and 60 °C, respectively) and hard-phase area density (1.4%, 5.8%, and 25.6% at 25, 40, and 60 °C). Tempering above 60 °C again decreased the size (118 and 100 nm, for 75 and 90 °C, respectively) and area coverage (16.4% and 12.1%, for 75 and 90 °C, respectively) of hard domains, likely as a result of the higher extent of network mobility and reduction in cross-linking density (Figure 3c,e,g). Finaly, tempering at temperatures above T_{UT} (110 °C) completely erased the phase separated morphology, in line with the expected large extent depolymerization and immiscibility to miscibility change between the two phases above T_{UT} (**Figure 5b**; Table S2, Supporting Information).[23] Remarkably, these changes in phase separation size and density was also reversible: heat treatment at 60 °C for 24 h after phase erasing at 130 °C was capable of partially recovering the DRIPS microstructure (Figure S27, Supporting Information), pointing toward a reprocessable materials with recovery of initial morphology and mechanical properties (vide infra).

The effect of the thermal tempering and hard-phase volume coverage was immediately apparent in the mechanical properties of the resulting materials, enabling to target an impressive wide range of E, stresses at break (σ_b), and elongations at break (ε_b) (Figure 4c; Table S3, Supporting Information). Initially, photocured materials stored at ambient temperature (below T_g, 1.4% hard area density) were rigid and ductile (E = 1.6 GPa, ε_b = 44%; σ_b = 21 MPa; ε_{yield} = 2.5%; σ_{yield} = 29 MPa), while they became more brittle upon tempering below the onset of T_{UT} affording

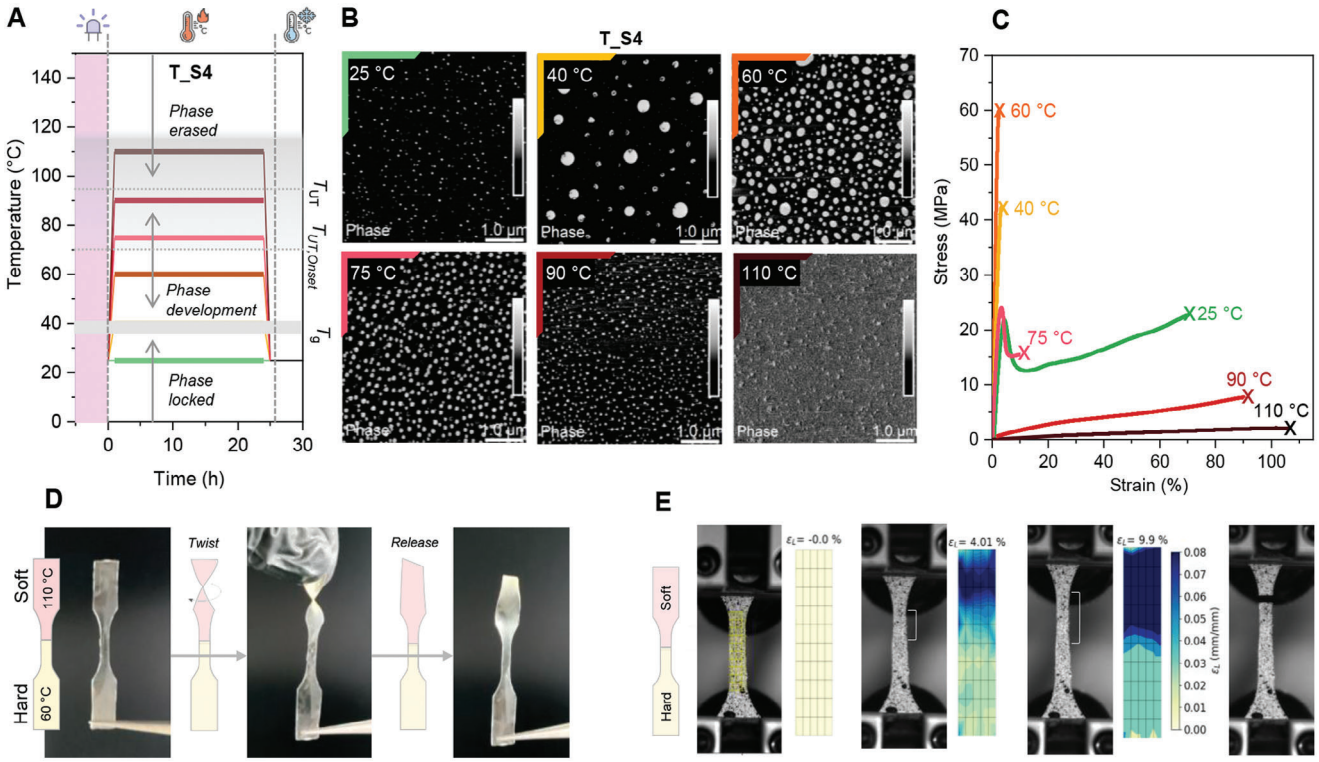

Figure 4. a) Scheme of the applied thermal treatment to **T_S4**: 1) UV-photocuring of the monomer resin (30 min), 2) annealing at various temperatures (25 °C (green), 40 °C (yellow), 60 °C (orange), or 110 °C (dark red) for 24 h), and 3) cooling to room temperature. b) Atomic force microscopy (AFM) imaging of **T_S4** after thermal annealing. c) Representative uniaxial tensile testing data of **T_S4** specimens (ASTM dogbone Type V) after different heat treatments (10 mm min^{-1}). d) Demonstration of local annealing on a dogbone specimen by applying torque. e) Application of a tensile stress to a locally annealed dogbone, displaying larger extensibility in the soft section and corresponding strain field.

materials that are stiff (E increased by ×1.1 and ×1.9, ε_b decreased by ×0.09 and ×0.06, and σ_b increased by ×2.1 and ×2.6, at 40 and 60 °C, respectively). Within this tempering window, the increased density of hard domains (5.8%, and 25.6%) restricted the mobility of the polymer network in a similar manner as a (nano) fillers can strengthen a matrix.[58,59] Mirroring the decrease of size and area coverage of hard domains above the onset of T_{UT} observed in the AFM, tempered materials at 75 and 90 °C where respectively softer (E = 1 GPa, ε_b = 12.5%; σ_b = 15.5 MPa; ε_{yield} = 3.3%; σ_{yield} = 24 MPa) and elastomeric without a yield point (E = 11.7 MPa, ε_b = 88%; σ_b = 7.7 MPa). Finally, when the material was treated at temperatures above T_{UT} (Figure 4-b) an even softer elastomeric material was obtained (E = 2 MPa, ε_b = 108%; σ_b = 2 MPa), that displayed elastic recovery above 95% over ten stretching cycles (Figure S28, Supporting Information). This simple tempering procedure enabled to reach properties from elastomeric to rigid plastics from a single pluripotent material in a wider range in respect to previous studies.[26]

Previously, locally graded mechanical properties were achieved with multimaterial design in FDM to achieve multi-performance objects.[60] Pluripotent materials have the potential to achieve the same feat but without the complexity of multimaterial printing.[8,61] To demonstrate this ability, we prepared a dogbone sample with a rigid side (60 °C, 24 h) and a softer side (110 °C, 4 h). When applying torque, only the soft side responded to the stimulus by cork-screw twisting (Figure 4d). Upon release of the stress, the sample elastically returned to the initial state. A similarly treated specimen was subjected to a uniaxial tensile test. Digital image correlation was used to compute the global strain field and thus identify the difference in mechanical behavior of the two regions (Figure 4e). Upon a global strain of 4.0%, the upper part deformation was 6.1% when the lower rigid part only deformed of 1.1%. As expected, the deformation and final rupture were localized in the softer region, proving that locally controlled mechanical properties were achievable through spatially resolved annealing.

To further investigate the effect of cross-linking density on the mechanical properties of the materials, we extended the network synthesis to tri-functional (lower cross-linking density) and hexa-functional (higher cross-linking density) poly-thiols (Trimethylolpropane tris(3-mercaptopropionate)), S3, and dipentaerythritol hexakis(3-mercaptopropionate), S6). Using equimolar amounts of AllOx with S3 or S6, both radical (**R_S3** and **R_S6**) and tandem (**T_S3** and **T_S6**) networks were photocured under identical conditions of photoinitiation as those employed with tetra-thiol S4. Supporting Information includes detailed explanation and thermomechanical and spectroscopic characterizations, which confirmed the consumption of all the C=C (allyl and alkylidene) groups upon irradiation (Figure S29, Supporting Information). Similarly to **T_S4**, DRIPS microstructures (a dual phase morphology with circular domains embedded in a continuous matrix as determined by AFM (Figure 5a; Table S4, Supporting

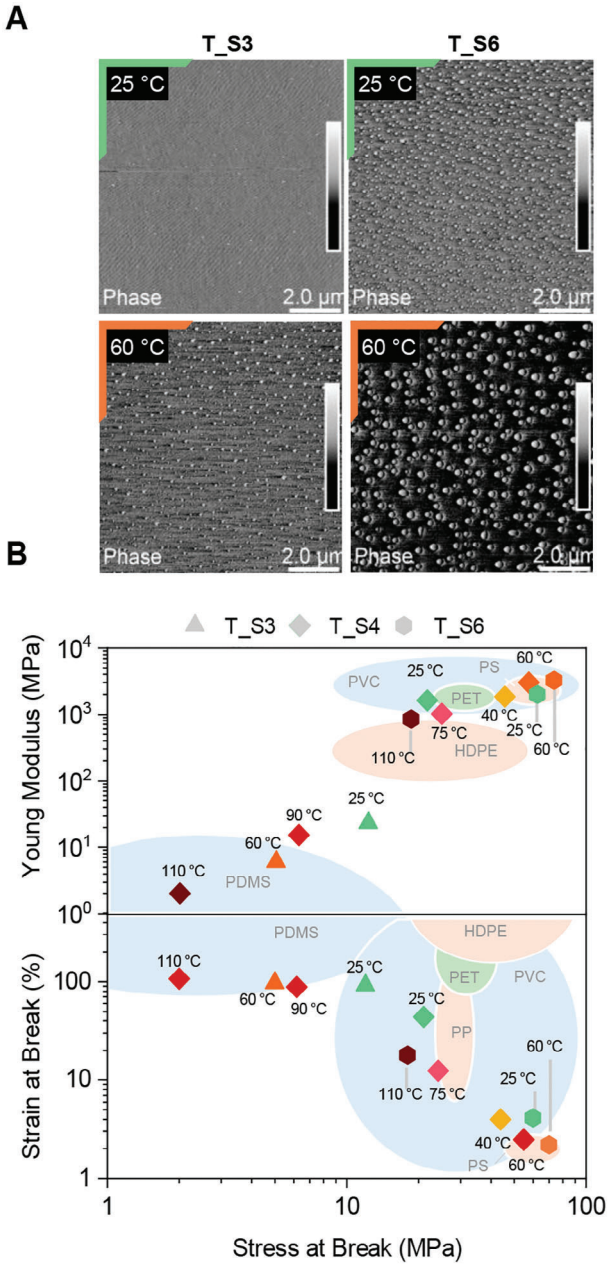

Figure 5. a) Atomic force microscopy (AFM) imaging of **T_S3** and **T_S6** after thermal annealing at 25 °C (green) and 60 °C (orange) for 24 h. b) Ashby plot of uniaxial tensile data for materials studied in this work.

Information), and two thermal transitions (T_g = 9–44 °C, $T_{UT,Onset}$ = 33–60 °C, T_{UT} = 80–118 °C, for **T_S3** and **T_S6**, respectively; Figure S30, Supporting Information) were present in both tandem materials. Again, the phase morphology was greatly dependent on the $T_{tempering}$ and its relative position with respect to T_g, $T_{UT,onset}$, and T_{UT} (Table S4, Supporting Information). Hence, **T_S3** displayed no detectable phase separation at ambient temperature, and only a sparse number of small spherical domains were observed (48 nm, 1.9% of the area) after annealing at 60 °C. In contrast, **T_S6** already showed a large number of quasi-spherical domains at ambient temperature (84 nm, 6% hard-phase area density), which greatly increased in size and area coverage upon heat treatment at 60 °C (600 nm, 15% hard-phase area density). Regardless of their $T_{tempering}$, **T_S3** and **T_S6** were found to be amorphous due to the lack of crystalline features observed in the X-Ray diffractograms (Figure S31, Supporting Information). In contrast, radical networks (**R_S3** and **R_S6**) had no DRIPS microstructures, given the presence of a single thermal transition (T_g = −7 and 41 °C for **R_S3** and **R_S6**, respectively, Figure S32, Supporting Information).

The network cross-linking density not only influenced the submicron morphology but as expected, gave stark differences in mechanical properties. As expected, given its lower cross-linking density, **T_S3** was softer when compared to **T_S4** while **T_S6** was more rigid owing to a higher network density. The effect of **T_S3** and **T_S6** tempering was demonstrated after annealing at three different temperatures (25, 60, 110 °C) (Figure S33, Supporting Information); full mechanical characterization is presented in Table S3 (Supporting Information). Taking all tandem materials (**T_S3**, **T_S4**, **T_S6**), the range of obtained properties expanded thanks to the combination of pluripotency and the tuning of the network density (Figure 5b): 3-orders of magnitude in E (2 MPa to 3.3 GPa), 2-orders of magnitude in ε_b (2% to 108%), and 1-order of magnitude in σ (2 MPa to 70 GPa). In comparison, the range of tensile properties attained by the radical networks (**R_S3**, **R_S4**, **R_S6**), which are not responsive to tempering, were substantially narrower (Table S3, Supporting Information). The combined results from spectroscopic and mechanical analyses suggest that, contrasting with previously studied thia-Michael networks, the mechanical properties of tandem oxazolidone-based cross-linked materials are governed by a combination of phase separation and cross-linking density (extent of adduct formation).[26]

While recycling has been proven for other homogenous, single-phase *N,S*-acetal-based materials on the basis of their reversible thiol-ene reaction,[33] we wanted to understand the influence of the phase separation on polymer flow and potential reprocessability of the dynamic thermosets. To rationalize these effects, we first measured stress relaxation of **T_S4** after treatment above T_{UT} (110 °C, 24 h, Figure S34a, Supporting Information), where phase separation was erased, and compared with a **T_S4** sample with a fully developed dual phase morphology (60 °C, 24 h, **Figure 6a**). Analyses on heating from 70 °C upwards in a timescale that would not interfere with the DRIPS microstructure, uncovered that, in fact, the flow activation energy (E_{flow}) for both samples to be similar (74 kJ mol^{-1}, Figure 6B; Figure S34b, Supporting Information), values within range of previously reported cationic-mediated and anionic-mediated thio-ene and thio-Michael networks.[26,33] Importantly, while the E_{flow} did not vary between the two, we found a difference in the relaxation times (Table S5, Supporting Information).

Indeed, the phase separated material displayed ×1.3–1.6 slower relaxation times at the measured temperatures, a phenomenon previously reported for other phase separated systems.[62] This behavior can be explained on the basis of hard domains hindering bond exchange by trapping part of the dynamic linkages and/or acting as a physical barrier for exchange.[63,64]

We then studied the mechanical recyclability of the tandem materials by grinding a sample of photocured **T_S4** and hot pressing for 3 min at 100 °C under 1 ton of pressure. Under

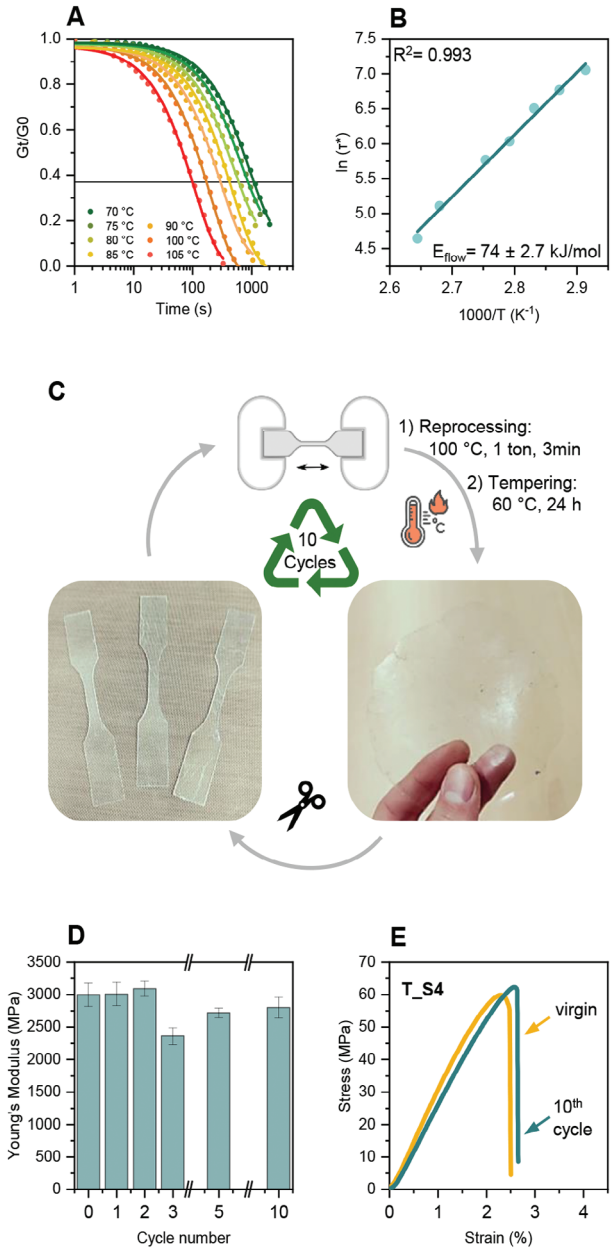

Figure 6. a) Stress relaxation of the tandem material **T_S4** with fully developed phase morphology (previously tempered at 60 °C, 24 h), lines are fitted first order Maxwellian. b) Arrhenius plot of relaxation times versus temperature for tempered tandem material **T_S4**. c) recycling process d) Evolution of Young's Modulus over 10 recycling cycles. e) Stress–Strain curves of virgin and recycled tandem material.

these conditions, colorless, transparent, and homogeneous films were obtained (**Figure** 7c). To re-introduce a developed DRIPS microstructure, the films were then subsequently treated at 60 °C for 24 h. After 10 recycling cycles, the mechanical properties remained practically unchanged with E remaining between 3.0–2.8 GPa (Figure 7d,e). The material did not show any discoloration and its IR spectrum and DSC trace were unchanged after 10 cycles (Figure S35a,b, Supporting Information), suggesting that the material did not degrade during reprocessing. These results are quite remarkable, as it implies that the cationic-mediated mechanism necessary for the reversible thiol-ene reaction remained functioning after many reprocessing cycles, suggesting no decomposition of any catalytic protic species.

5. FDM of Pluripotent Materials toward Functional Builds

The melt-flow properties of depolymerized networks above T_{UT} (>100 °C), which enabled the reprocessing of solid films, enticed the prospect of applying the tandem dynamic networks in filament-based additive manufacturing. For adequate printability, materials are required to display: i) complex viscosities below 10^3 Pa·s at reasonable printing temperatures, and ii) significant shear thinning, since it allows exiting the nozzle easily and retaining the shape after deposition, resulting in high definition and controlled flow.[17,65] Viscosity measurements by shear-rheology determined that **T_S4** and **T_S6** displayed shear thinning in all tested temperatures, ranging from 100–150 and 160–190 °C, respectively (Figure 7a; Figures S36 and S37, Supporting Information). Moreover, complex viscosities at high frequencies (at 100 Hz) were well within the printability region, revealing a desirable rheological behavior for FDM.[66]

While pellet extrusion has some inherent challenges such as the need for a consistent material flow,[67] we selected this technology as it is closer to commercial models and has been regarded as a strong tool in the industrialization of FDM printing.[68–71] As a proof of concept, pieces of photocured **T_S6** were extruded through a twin screw extruder at 165 °C into filaments of 2 mm in diameter, which were subsequently pelletized into fragments between 3–5 mm in size (Figure S38, Supporting Information). A minor change in coloration from yellow to dark yellow was noted, possibly due to thermal degradation of the materials. The pellets were fed into a modified Ender 3 NEO printer fitted with a v4 universal pellet extruder and a 0.4 mm nozzle heated to 150 °C (Figure 7b; Figure S39, Supporting Information). Under these printing conditions (0.2 mm layer, 7.5 mm s^{-1}, 50% infill), a single walled geometric vase structure, a complex spiral vase, and a pyramid were printed measuring several centimeters (Figure 7c, top, Figure S40, Supporting Information for a zoomed version). The selected infill had reasonable resolution; small variations were observed in the Z-axis as a result of inconsistent flow due to the complex single-screw system that fed the nozzle.[70] Importantly, the printed objects displayed significant interlayer cohesion as shown in scanning electron microscopy (SEM) images (Figure 7c, bottom), highlighting the bridging ability of **T_S6** after deposition.

This observation prompted us to investigate the ability of printed tandem materials to produce isotropic prints. In traditional FDM, weak non-covalent forces between different layers results in poor interfilamentous adhesion and significant anisotropic mechanical properties.[8,9] This has significantly limited the industry adoption of FDM to small-scale and bespoke prototyping tool. Addressing this challenge has been highlighted as a key advancement toward expanding 3D printing toward functional applications, in a market that is projected to grow to 1$ trillion by 2030.[21] To demonstrate this, 2.5D rectangular structures of **T_S4** were printed with a single-filament direction, and subsequently rigidified at 60 °C for 24 h. Analyses by DMTA showed

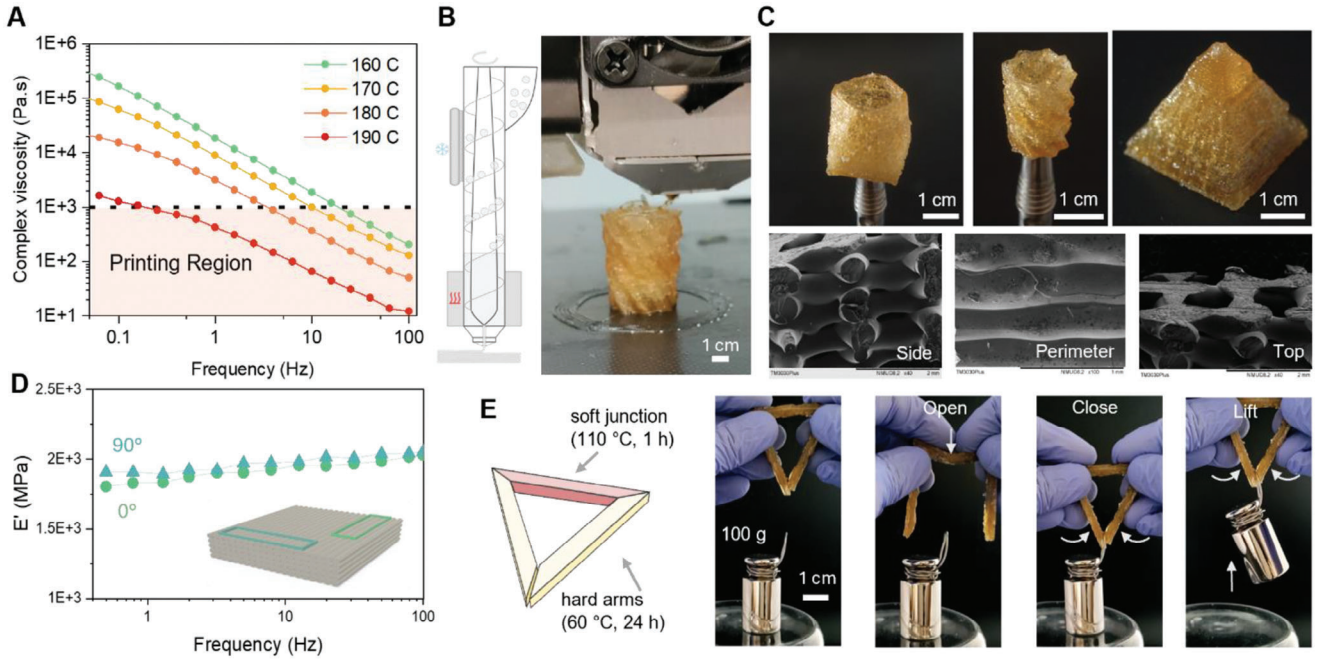

Figure 7. a) Plot of complex viscosity versus frequencies of **T_S6** at temperatures ranging from 160 to 190 °C obtained by melt shear rheology. b) Diagram of the FDM printing head with pellet extrusion and photography of the printing process of **T_S6**. c) Top: photographs of 3D printed single-walled geometric vase (left), spiraling vase (center), and pyramid (right) with 50% infill. Bottom: scanning electron microscopy (SEM) images of cut sections of **T_S6** printed object by extrusion FDM. d) Frequency sweeps of 3D printed specimens (**T_S4**) perpendicular and parallel to the bead orientation e) Scheme of functional gripper with spatially resolved mechanical properties, and demonstration of a 3D-printed functional gripper that exploits areas of distinct rigidity to lift a weight (arrows show the direction and location of the applied forces).

no significant difference in *E'* as measured in the 0° and 90° orientation with respect to the filaments highlighting its isotropic behavior (Figure 5d).[17]

As a final proof of the ability of thiol-ene based printed thermosets to display localized mechanical properties, a simple gripper was printed and locally heated to have a soft junction that connected two rigid arms (Figure 5e). First, the object was tempered at 60 for 24 h to completely rigidify it; then, the connecting bar was locally heated over a hot plate at 110 °C for 1 h to provide the elastic section. As a result of this treatment, the gripper was able to open and close effortlessly when actuated manually through the bending of the middle section and hold and lift a weight of 100 g with the tip of the rigid arms. The ability to have spatially-resolved mechanical properties has a high potential to impact the fields of compliant mechanics and soft robotics.[72]

6. Conclusion

We have presented a new strategy for the production of pluripotent materials that enables their introduction in the field of additive manufacturing. With this strategy we attain properties ranging from Young's Moduli of 2 MPa and elongation at break of 100% toward moduli of 3 GPa and stress at break of 55 MPa with a single resin. By exploiting two double bonds with different reactivity, the monomer could form a mixture of dynamic *N,S*-acetals and non dynamic thioether moieties that cascaded toward desirable viscoelastic properties showing both shear thinning behavior and complex viscosity apt for FDM printing. Furthermore, they gave isotropic prints owing to the strong covalent bonding between filaments. Importantly, the materials presented a dynamic reaction-induced phase-separation (DRIPS) mechanism that could be exploited to tune the properties by simple thermal annealing in a fully reversible manner. As a proof of concept, we created a functional gripper with spatially resolved mechanical properties by simple localized heating, presenting a new paradigm for achieving functionality in 3D printing. The efficient reprocessability of the *N,S*-acetal moiety was further demonstrated by mechanical recycling the material for 10 cycles, resulting in a minor reduction in mechanical properties. The wide window of mechanical properties reveals the potential of the concept of pluripotency for the production of next-gen 3D printing materials, with deep implication in compliant mechanics and soft robotics.

Supporting Information

Supporting Information is available from the Wiley Online Library or from the author.

Acknowledgements

The authors would like to thank Prof. PhD Itziar Otaegi for their support in mechanical characterization and PhD Lucas Polo de Fonseca for the help in characterizing the phase behavior of the tandem materials. The authors thank for the technical and human support provided by SGIker (UPV/EHU/ ERDF, EU). The authors would like to express thanks for the financial support provided by the NIPU-EJD project; this project has received funding from the

European Union's Horizon 2020 research and innovation program under Marie Skłodowska-Curie Grant Agreement No. 955700. C.D. is FNRS Research Director and thanks FNRS for financial support in the frame of the CO2Switch project under grant T.0075.20. A.J.M. acknowledges the financial support from the Basque Government through grant IT1503-22. The authors acknowledge grant TED2021-129852B-C22 funded by MCIU/AEI/10.13039/501100011033 and by the European Union NextGenerationEU/PRTR and the grant PID2022-138199NB-I00 funded by MCIU/AEI/10.13039/501100011033. D.M. thanks Ayuda RYC2021-031668-I funded by MCIN/AEI/10.13039/501100011033 and by EU NextGenerationEU/PRTR.

Conflict of Interest

The authors declare no conflict of interest.

Author Contributions

M.C., F.V., D.M., C.D., and H.S. performed conceptualization; M.C., G.S., and F.V. performed data Curation; M.C. performed formal analysis; M.C., F.V., G.S., M.C.Q, L.I., and M.F. performed investigation; M.C., D.M., F.V., and H.S. methodology; M.C., F.V., and H.S. performed project administration; M.C.Q., L.I., M.F., and A.J.M. acquired resources; F.V., H.S., and C.D. performed validation; H.S., D.M., F.V., X.L.P., C.D., N.A., and J.M.R. performed Supervision; M.C., F.V., H.S., and D.M. wrote the original draft; T.H., B.G., A.J.M, N.A., and X.L.P. reviewed and edited the final manuscript; H.S, C.D., N.A., and J.M.R. performed funding acquisition.

Data Availability Statement

The data that support the findings of this study are available in the supplementary material of this article.

Keywords

3D printing, dissociative thermoset, FDM, phase separation, pluripotent material

Received: November 10, 2024
Revised: January 23, 2025
Published online: March 2, 2025

[1] A. K. Pal, A. K. Mohanty, M. Misra, *RSC Adv.* **2021**, *11*, 36398.
[2] S. A. M. Tofail, E. P. Koumoulos, A. Bandyopadhyay, S. Bose, L. O'Donoghue, C. Charitidis, *Mater. Today* **2018**, *21*, 22 .
[3] N. Shahrubudin, T. C. Lee, R. Ramlan, *Procedia Manuf.* **2019**, *35*, 1286.
[4] F. P. W. Melchels, M. A. N. Domingos, T. J. Klein, J. Malda, P. J. Bartolo, D. W. Hutmacher, *Prog. Polym. Sci.* **2012**, *37*, 1079 .
[5] S. Singh, S. Ramakrishna, *Curr. Opin. Biomed. Eng.* **2017**, *2*, 105 .
[6] I. J. Solomon, P. Sevvel, J. Gunasekaran, *Mater. Today Proc.* **2020**, *37*, 509 .
[7] Z. Jiang, B. Diggle, M. L. Tan, J. Viktorova, C. W. Bennett, L. A. Connal, *Adv. Sci.* **2020**, *7*, 1.
[8] V. Bijalwan, S. Rana, G. J. Yun, K. P. Singh, M. Jamil, S. Schlögl, *Polymer Rev.* **2024**, *64*, 36.
[9] S. H. Ahn, M. Montero, D. Odell, S. Roundy, P. K. Wright, *Rapid Prototyp. J.* **2002**, *8*, 248.
[10] M. A. Lucherelli, A. Duval, L. Avérous, *Prog. Polym. Sci.* **2022**, *127*, 101515.
[11] J. Zheng, Z. M. Png, S. H. Ng, G. X. Tham, E. Ye, S. S. Goh, X. J. Loh, Z. Li, *Mater. Today* **2021**, *51*, 586.
[12] N. J. Van Zee, R. Nicolaÿ, *Prog. Polym. Sci.* **2020**, *104*, 101233 .
[13] K. Kumar, T. J Dickens, *J. Appl. Polym. Sci.* **2023**, *140*, 1 .
[14] J. Joe, J. Shin, Y. Choi, J. Hwang, S. Kim, J. Han, B. Park, W. Lee, S. Park, Y. Kim, D. Kim, *Adv. Sci.* **2021**, *8*, 1 .
[15] S. Choi, B. Park, S. Jo, J. H. Seo, W. Lee, D.-G. Kim, K. B. Lee, Y. S. Kim, S. Park, *Adv. Eng. Mater.* **2022**, *24*, 1 .
[16] G. Prasanna Kar, X. Lin, E. M. Terentjev, *ACS Appl. Polym. Mater* **2022**, *4*, 4364 .
[17] M. C. Montoya-Ospina, J. Zeng, X. Tan, T. A. Osswald, *Polymers* **2023**, *15*, 1332 .
[18] S. Kim, M.d A. Rahman, M.d Arifuzzaman, D. B. Gilmer, B. Li, J. K. Wilt, E. Lara-Curzio, T. Saito, *Sci. Adv.* **2022**, *8*, 1 .
[19] M. O. Saed, X. Lin, E. M. Terentjev, *ACS Appl. Mater. Interfaces* **2021**, *13*, 42044 .
[20] K. Yang, J. C. Grant, P. Lamey, A. Joshi-Imre, B. R. Lund, R. A. Smaldone, W. Voit, *Adv. Funct. Mater.* **2017**, *27*, 1700318 .
[21] J. R. Davidson, G. A. Appuhamillage, C. M. Thompson, W. Voit, R. A. Smaldone, *ACS Appl. Mater. Interfaces* **2016**, *8*, 16961 .
[22] G. A. Appuhamillage, J. C. Reagan, S. Khorsandi, J. R. Davidson, W. Voit, R. A. Smaldone, *Polym. Chem.* **2017**, *8*, 2087 .
[23] K. M. Herbert, P. T. Getty, N. D. Dolinski, J. E. Hertzog, D. de Jong, J. H. Lettow, J. Romulus, J. W. Onorato, E. M. Foster, S. J. Rowan, *Chem. Sci.* **2020**, *11*, 5028 .
[24] S. Sivakova, D. A. Bohnsack, M. E. Mackay, P. Suwanmala, S. J. Rowan, *J. Am. Chem. Soc.* **2005**, *127*, 18202 .
[25] K. M. Herbert, N. D. Dolinski, N. R. Boynton, J. G. Murphy, C. A. Lindberg, S. J. Sibener, S. J. Rowan, *ACS Appl. Mater. Interfaces* **2021**, *13*, 27471.
[26] N. R. Boynton, J. M. Dennis, N. D. Dolinski, C. A. Lindberg, A. P. Kotula, G. L. Grocke, S. L. Vivod, J. L. Lenhart, S. N. Patel, S. J. Rowan, *Science* **2024**, *383*, 545.
[27] Y. Jia, J. Qian, S. Hao, S. Zhang, F. Wei, H. Zheng, Y. Li, J. Song, Z. Zhao, *Adv. Mater.* **2024**, *36*, 2313164.
[28] K. Ehrmann, C. Barner-Kowollik, *J. Am. Chem. Soc.* **2023**, *145*, 24438.
[29] J. J. Schwartz, A. J. Boydston, *Nat. Commun.* **2019**, *10*, 1 .
[30] L. Y. Zhou, J. Fu, Y. He, *Adv. Funct. Mater.* **2020**, *30*, 1 .
[31] M. A. S. R. Saadi, A. Maguire, N. T. Pottackal, Md. S. H. Thakur, M. Md. Ikram, A. J. Hart, P. M. Ajayan, M. M. Rahman, *Adv. Mater.* **2022**, *34*, 2108855.
[32] K. L. Sampson, B. Deore, A. Go, M. A. Nayak, A. Orth, M. Gallerneault, P. R. L. Malenfant, C. Paquet, *ACS Appl. Polym. Mater* **2021**, *3*, 4304 .
[33] T. Habets, G. Seychal, M. Caliari, J.-M. Raquez, H. Sardon, B. Grignard, C. Detrembleur, *J. Am. Chem. Soc.* **2023**, *145*, 25450.
[34] S. Laviéville, C. Totée, P. Guiffrey, S. Caillol, C. Bakkali-Hassani, V. Ladmiral, E. Leclerc, *Macromolecules* **2024**, *57*, 10311.
[35] B. P. Sutherland, M. Kabra, C. J. Kloxin, *Polym. Chem.* **2021**, *12*, 1562.
[36] M. Uchiyama, M. Osumi, K. Satoh, M. Kamigaito, *Angew. Chem.–Int. Ed.* **2020**, *59*, 6832.
[37] Q. Li, S. Ma, N. Lu, J. Qiu, J. Ye, Y. Liu, S. Wang, Y. Han, B. Wang, X. Xu, H. Feng, J. Zhu, *Green Chem.* **2020**, *22*, 7769 .
[38] T. Habets, F. Siragusa, B. Grignard, C. Detrembleur, *Macromolecules* **2020**, *53*, 6396 .
[39] B. Grignard, S. Gennen, C. Jérôme, A. W. Kleij, C. Detrembleur, *Chem. Soc. Rev.* **2019**, *48*, 4466 .
[40] S. Gennen, B. Grignard, T. Tassaing, C. Jérôme, C. Detrembleur, *Angew. Chem. – Int. Ed.* **2017**, *56*, 10394.
[41] T. Habets, F. Siragusa, A. J. Müller, Q. Grossman, D. Ruffoni, B. Grignard, C. Detrembleur, *Polym. Chem.* **2022**, *13*, 3076.
[42] A. Pal, A. R. Wong, J. R. C. R. Lamb, *ACS Macro Lett.* **2024**, *13*, 502.
[43] S. Maes, T. Habets, S. M. Fisher, B. Grignard, C. Detrembleur, F. E. Du Prez, *Polym. Chem.* **2024**, *8*, 5255.

[44] M. Razavi-Esfali, T. Habets, F. Siragusa, B. Grignard, H. Sardon, C. Detrembleur, *Polym. Chem.* **2024**, *15*, 1962 .
[45] F. Vidal, E. R. van der Marel, R. W. F. Kerr, C. McElroy, N. Schroeder, C. Mitchell, G. Rosetto, T. T. D. Chen, R. M. Bailey, C. Hepburn, C. Redgwell, C. K. Williams, *Nature* **2024**, *626*, 45 .
[46] C. Hepburn, E. Adlen, J. Beddington, E. A. Carter, S. Fuss, N. Mac Dowell, J. C. Minx, P. Smith, C. K. Williams, *Nature* **2019**, *575*, 87 .
[47] H. Jiang, J. Zhao, A. Wang, *Synthesis* **2008**, *5*, 763 .
[48] C. J. Stubbs, A. L. Khalfa, V. Chiaradia, J. C. Worch, A. P. Dove, *J. Am. Chem. Soc.* **2022**, *144*, 11729 .
[49] C. Shi, R. W. Clarke, M. L. McGraw, E. Y. X. Chen, *J. Am. Chem. Soc.* **2022**, *144*, 2264 .
[50] T. Ebert, A. Wollbrink, A. Seifert, R. John, S. Spange, *Polym. Chem.* **2016**, *7*, 6826 .
[51] M. Uygun, M. A. Tasdelen, Y. Yagci, *Macromol. Chem. Phys.* **2010**, *211*, 103 .
[52] T. Habets, G. Seychal, M. Caliari, J.-M. Raquez, H. Sardon, B. Grignard, C. Detrembleur, *J. Am. Chem. Soc.* **2023**, *145*, 25450 .
[53] J. V. Crivello, *J. Polym. Sci. A Polym. Chem.* **1999**, *37*, 4241.
[54] O. Konuray, X. Fernández-Francos, X. Ramis, À. Serra, *Polymers* **2018**, *10*, 178 .
[55] M. Invernizzi, R. Suriano, A. Muscatello, S. Turri, M. Levi, *J. Appl. Polym. Sci.* **2020**, *137*, 48333 .
[56] Y. Yagci, S. Jockusch, N. J. Turro, *Macromolecules* **2010**, *43*, 6245 .
[57] L. Pierau, C. Elian, J. Akimoto, Y. Ito, S. Caillol, D.-L. Versace, *Prog. Polym. Sci.* **2022**, *127*, 101517 .
[58] A. J. Crosby, J. Y. Lee, *Polymer Reviews* **2007**, *47*, 217 .
[59] C. R. López-Barrón, J. Lu, J. A. Throckmorton, H. Passino, M. M. Gopinadhan, *Macromolecules* **2024**, *57*, 2729 .
[60] D. Espalin, J. A. Ramirez, F. Medina, R. Wicker, *Rapid Prototyp. J.* **2014**, *20*, 236 .
[61] A. Nazir, O. Gokcekaya, K. Md Masum Billah, O. Ertugrul, J. Jiang, J. Sun, S. Hussain, *Mater. Des.* **2023**, *226*, 111661 .
[62] R. G. Ricarte, F. Tournilhac, L. Leibler, *Macromolecules* **2019**, *52*, 432 .
[63] M. H. P. de Heer Kloots, S. K. Schoustra, J. A. Dijksman, M. M. J. Smulders, *Soft Matter* **2023**, *19*, 2857 .
[64] H. Han, X. Xu, *J. Appl. Polym. Sci.* **2018**, *135*, 1 .
[65] A. Dominguez-Alfaro, M. Criado-Gonzalez, E. Gabirondo, H. Lasa-Fernández, J. L. Olmedo-Martínez, N. Casado, N. Alegret, A. J. Müller, H. Sardon, A. Vallejo-Illarramendi, D. Mecerreyes, *Polym. Chem.* **2022**, *13*, 109 .
[66] R. Arrigo, A. Frache, *Polymers* **2022**, *14*, 1754 .
[67] B. M. Boyle, P. T. Xiong, T. E. Mensch, T. J. Werder, G. M. Miyake, *Addit. Manuf.* **2019**, *29*, 100811 .
[68] C. E. Duty, V. Kunc, B. Compton, B. Post, D. Erdman, R. Smith, R. Lind, P. Lloyd, L. Love, *Rapid Prototyp. J.* **2017**, *23*, 181 .
[69] F. A. Cruz Sanchez, H. Boudaoud, M. Camargo, J. M Pearce, *J. Clean Prod.* **2020**, *264*, 121602 .
[70] H. Liu, K. Gong, A. Portela, Z. Cao, R. Dunbar, Y. Chen, *Addit Manuf.* **2023**, *75*, 103744.
[71] A. Patti, *Macromol. Rapid Commun.* **2024**, *49*, 2400249.
[72] G. M. S. R Whitesides, *Angew. Chem. – Int. Ed.* **2018**, *57*, 4258.